ACS Sustainable Chemistry & Engineering

Research Article

Cite This: ACS Sustainable Chem. Eng. 2019, 7, 9007−9016

pubs.acs.org/journal/ascecg

# Ru@Pt Core−Shell Nanoparticles: Impact of the Atomic Ordering of the Ru Metal Core on the Electrocatalytic Activity of the Pt Shell

Jiasui Zou,[†] Min Wu,[†] Shunlian Ning,[†] Lin Huang,[†] Xiongwu Kang,*[,†] and Shaowei Chen[†,‡,§]

[†]Guangzhou Key Laboratory for Surface Chemistry of Energy Materials, New Energy Research Institute, School of Environment and Energy, South China University of Technology, 382 East Waihuan Road, Guangzhou 510006, China

[‡]Department of Chemistry and Biochemistry, University of California, 1156 High Street, Santa Cruz, California 95064, United States

Supporting Information

**ABSTRACT:** Constructing core−shell nanostructures is demonstrated to be an effective strategy to improve catalytic activity of metal nanoparticles. However, the impact of the atomic ordering of the metal core on the performance of the shell remains unexplored. Here, ruthenium−platinum (Ru−Pt) core−shell nanoparticles, with a crystalline and amorphous Ru core of the same diameter and diverse Pt shell thicknesses, are prepared and characterized by X-ray diffraction (XRD), X-ray photoelectron spectroscopy (XPS), high-angle annular dark-field scanning transition electron spectroscopy (HAADF-STEM), and CO tripping voltammetry. The well-defined heterostructured Ru−Pt interface and anisotropic growth of the Pt shell on the crystalline Ru core (Ru@Pt$_x$) were observed, while the amorphous Ru core induces a partial alloy at the Ru−Pt interface and isotropic growth of the Pt shell. The core−shell structure also results in an apparent down-shift of the d-band center of Pt, which dissipates much faster on the amorphous Ru core than on crystalline ones, as demonstrated by the XRD and CO desorption potential. The two sets of core−shell nanoparticles show that a volcano-shape dependence of the catalytic activity on the thickness of the Pt shell and the crystalline Ru core markedly enhanced the catalytic performance and stability toward electro-oxidation of formic acid and ethanol, which is ascribed to the lattice strain of the Pt shell, down-shift of the d-band center, the weakened CO adsorption, and thus alleviated poisoning.

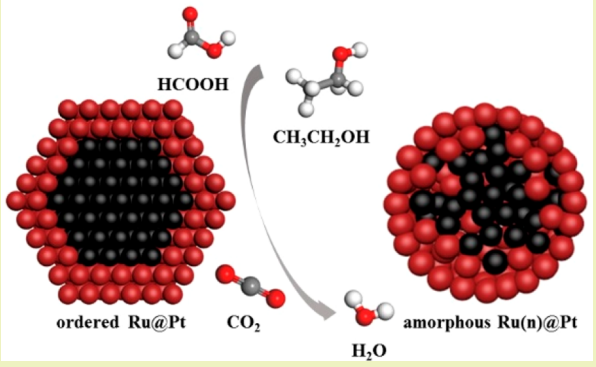


**KEYWORDS:** *CO poisoning, Strain, d-Band, Ethanol oxidation, Formic acid oxidation*

## INTRODUCTION

Proton exchange membrane fuel cells (PEMFCs) are considered a promising clean and renewable power source; however, massive commercialization is still largely limited by the high cost and fast deactivation of the cathode and anode catalysts.[1−3] Ru and Pt alloys have been demonstrated as an excellent anode catalyst,[4−6] where the ligand effect (electronic effect) and strain/packing effect[7−9] induced by Ru alloying are recognized to suppress the CO poisoning and promote the catalytic activity of Pt. However, the Pt−Ru alloy suffers from the feasible dissolution of Ru and fast attenuation of the catalytic activity upon potential cycling.[10−13]

Ru@Pt core−shell nanostructures have been equally demonstrated to be effective in improving the catalytic activity of the catalysts,[14] and the Ru substrate was recognized to be able to reduce the CO adsorption energy on Pt layers because of the strain effect from the Ru substrate[15,16] and further enhance the catalytic performance of Pt.[17−22] By following this, Alayoglu reported the selective oxidation of CO in a $H_2$ stream on Ru@Pt core−shell nanoparticles, and the enhanced catalytic activity was ascribed to the increased availability of CO-free Pt surface sites and the hydrogen-mediated low-temperature CO oxidation process.[18,23] Lately, Ehab and co-workers[24] prepared Ru@Pt core−shell nanoparticles by polyol reduction method at 220 °C and investigated the CO and formic acid oxidation, ascribing the enhanced catalytic activity to the electronic effect. However, both the large lattice defects of the amorphous Ru core and the deposition of the Pt shell at high temperatures (220 °C) can promote the formation of the Pt−Ru alloy at the Ru−Pt core−shell interface,[23,25] obscuring the effect of the Ru substrate on the Pt shell. It is highly possible for the atomic ordering of the Ru core to tune the lattice strain and the catalytic activity of the Pt shell, which yet remain unexplored.

Herein, Ru@Pt core−shell nanoparticles (NPs) with an ordered and amorphous Ru metal core (Scheme 1) of the same size and diverse thickness of the Pt shell are prepared systematically and further subjected to characterization of scanning transmission electron microscopy (STEM), XRD, XPS, and FTIR. It is observed that the Pt−Ru alloy was formed

Received: March 4, 2019
Revised: April 2, 2019
Published: April 3, 2019






DOI: 10.1021/acssuschemeng.9b01270
ACS Sustainable Chem. Eng. 2019, 7, 9007−9016

**Scheme 1. Intersection View of Ru@Pt Core–Shell Nanoparticles**[a]

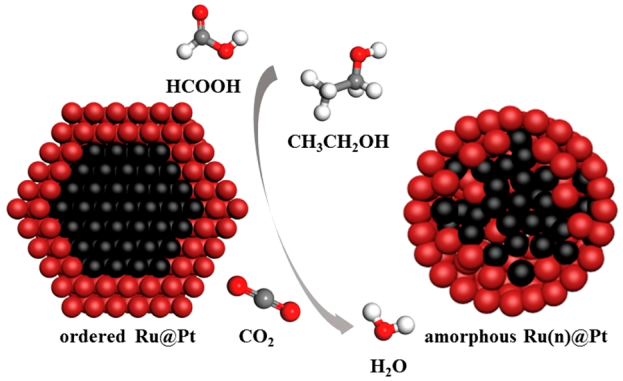


[a](Left) The ordered Ru metal core results in a well-defined Ru–Pt interface, and (right) the amorphous Ru metal core leads to an alloyed Ru–Pt interface. Black and dark red dots represent Ru and Pt atoms, respectively.

at the Ru@Pt interface on the amorphous Ru core, and the catalytic activity of core–shell nanostructures with the ordered Ru core was much higher than that of the amorphous Ru core, which was accounted for by the lattice strain and the down-shift of the d-band center induced by the ordered Ru core.

## EXPERIMENTAL SECTION

**Chemicals.** $H_2PtCl_6$ (99%), $RuCl_3$ (99%), Nafion (5%), ethanol (99%), formic acid (99%), perchloric acid (98%), and sodium hydroxide (97%) are purchased from Energy Chemistry and used as received. Commercial Pt/C (<5 nm Pt nanoparticles supported on carbon black) is from Sigma-Aldrich (Pt: 20 wt %). Deionized (DI) water was supplied by a Barnstead Nano pure water system (18.3 MΩ cm).

**Synthesis of CNT-Supported Ru@Pt Core–Shell Nanoparticles.** Carbon-nano-tube-supported (CNT-supported) Ru@Pt core–shell nanoparticles were prepared using a sequential ethanol reduction method. First, CNT-supported Ru NPs were synthesized by refluxing 100 mL of ethanol containing 0.4 mmol of $RuCl_3$ at 110 °C for 1 h. A 135 mg portion of CNTs was dispersed in ethanol solution by sonication for 1 h and then injected into the above reaction flask. Upon the temperature of the solution stabilizing at 110 °C, 6 mL of

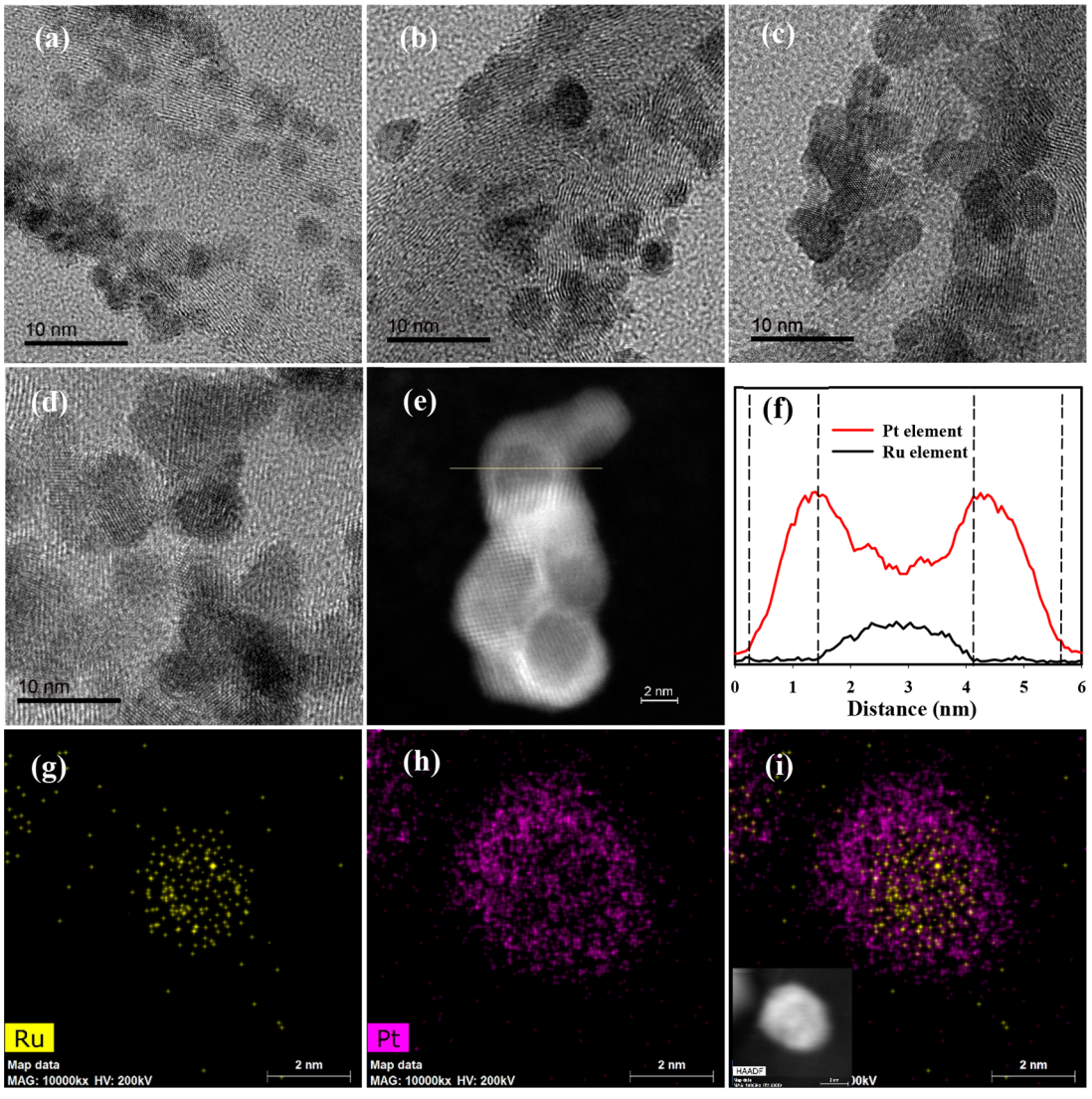


**Figure 1.** TEM images of $Ru@Pt_x$: (a) $x$ = 0.5, $D$ = 3.2 ± 0.4 nm; (b) $x$ = 0.75, $D$ = 3.9 ± 0.4 nm; (c) $x$ = 1.0, $D$ = 4.9 ± 0.7 nm; (d) $x$ = 1.25, $D$ = 6.8 ± 1.3 nm. HAADF-STEM image of (e) $Ru@Pt_{1.0}$ with (f) compositional line scan profile of Ru and Pt elements. HAADF-STEM elemental EDX-mapping images of (g) Ru, (h) Pt, and (i) overlap of Ru and Pt recorded along the inset HAADF-STEM image of $Ru@Pt_{1.0}$.



DOI: 10.1021/acssuschemeng.9b01270
ACS Sustainable Chem. Eng. 2019, 7, 9007–9016

**Table 1. Lattice Parameter and Strain of the Pt Shell for the Ru@Pt$_x$ and Ru(n)@Pt$_x$ Nanoparticles**

| | Ru@Pt$_x$ | | | | Ru(n)@Pt$_x$ | | | |
|---|---|---|---|---|---|---|---|---|
| $x$ | 0.5 | 0.75 | 1.0 | 1.25 | 0.5 | 0.75 | 1.0 | 1.25 |
| $a$[a] (Å) | 3.877 | 3.880 | 3.884 | 3.887 | 3.860 | 3.889 | 3.894 | 3.909 |
| Pt strain | −0.869 | −0.798 | −0.694 | −0.609 | −0.639 | −0.543 | −0.439 | −0.156 |
| $D$[b] (nm) | 3.2 | 3.9 | 4.9 | 6.8 | | | 4.5 | |
| Pt layers | 1.2 | 2.5 | 4.3 | 7.7 | | | 3.6 | |

[a]$a$: Lattice parameter. [b]$D$: diameter.

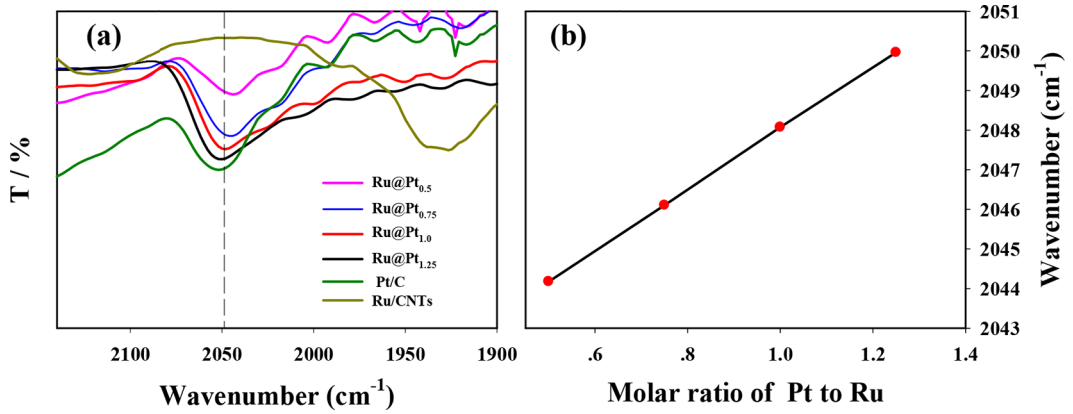


**Figure 2.** (a) FTIR spectra of Ru/CNTs, Pt/C, and Ru@Pt$_x$ nanoparticles with adsorbed CO. (b) Dependence of the vibrational band of nanoparticle-adsorbed CO on the molar ratio of Pt to Ru. The FTIR spectra for Ru(n)@Pt$_x$ are shown in Figure S3.

0.2 M NaOH (in ethanol or water) was injected quickly. After 2 hours, an extra 0.2 mmol of 0.2 M NaOH was injected to ensure complete reduction of $Ru^{3+}$. The solution was further refluxed for another 30 min, and the nanocomposites were precipitated by centrifugation and dried in vacuum. The as-synthesized Ru nanoparticles supported on CNTs had an amorphous Ru metal core and were denoted as Ru(n), which was further annealed under $H_2$/Ar mixed gas at 450 °C for 1 h in a tube furnace to make the crystalline Ru core. For the fabrication of Ru−Pt core−shell structures, crystalline and amorphous Ru supported on CNTs was then dispersed in 100 mL of ethanol and refluxed at 110 °C for 1 h, respectively. A certain amount of $H_2PtCl_6$ in 8 mL of ethanol with an atomic ratio of Pt to Ru of $x$ ($x$ = 0.5, 0.75, 1.0, and 1.25) was transferred into the mixture and refluxed at 110 °C for another 2 h under vigorous stirring at room temperature. An additional amount of 0.2 M NaOH aqueous solution (up to double $Pt^{2+}$) was added for complete reduction of $H_2PtCl_6$. The final products were labeled as Ru@Pt$_x$ or Ru(n)@Pt$_x$, respectively. The sizes of crystalline and amorphous Ru cores are tuned to be similar to each other by controlling the NaOH addition rate. Consequently, Ru(n)@Pt$_x$ and Ru@Pt$_x$ nanoparticles share the same Ru core size and Pt shell thickness when the molar ratio of Pt to Ru is set. The atomic ratio of Pt to Ru of Ru@Pt$_x$ is further characterized by ICP-AES, which is in good agreement with the stoichiometric ratio. The mass loading of Pt on each sample was set to be 24.9 wt %.

**Characterization.** The diameter of nanoparticles was determined by using TEM (JEOL TEM-2010), and the high-angle annular dark-field STEM (HAADF-STEM) images and line scanning were acquired on a Titan Themis 200 S/TEM instrument. The XRD was performed on a Bruker D8 diffractometer using a Cu K$\alpha$ source ($\lambda$ = 0.1541 nm) operating at 40 kV and 40 mA. The X-ray photoelectron spectroscopy (XPS) was recorded with a Phi X-tool instrument, and Fourier-transform infrared spectroscopy (FTIR) was measured on a Nicolet 6700 instrument. Ru@Pt NP catalysts were dispersed in 15 mL of aqua regia ($HNO_3$/HCl) for 3 h at 150 °C, assisted by microwave technology (2450 MHz), to dissolve Ru NPs completely. Then, the resulting solutions were analyzed by inductively coupled plasma optical emission spectroscopy to obtain the Ru and Pt contents.

**Electrochemical Characterization.** For 2 mg $L^{-1}$ homogeneous catalyst ink, Ru@Pt$_x$, Ru(n)@Pt$_x$, or Pt/C was dispersed in ethanol solution and sonicated for 1 h. Then, 10 $\mu$L of catalyst ink was dropped on a glassy carbon electrode (5 mm in diameter). After the solvent was evaporated naturally in air, 4 $\mu$L of 5 wt % Nafion was drop-cast on top of the catalyst and dried naturally in air. The electrochemical performance was measured on a CHI-650E electrochemical workstation (CH Instruments Inc.) by using a standard three-electrode cell. The catalyst-covered GC electrode, saturated calomel electrode (SCE), or mercury/mercurous oxide electrode (Hg/HgO) was employed as the working and reference electrode, and the platinum-wire electrode was used as the counter electrode. Cyclic voltammetry (CV) was performed in 0.5 M $HClO_4$ aqueous solution from 0.05 to 1.0 V (versus reversible hydrogen electrode, RHE) to activate the catalyst and evaluate the electrochemical surface area (ECSA) by using underpotential deposition of hydrogen.[26,27] The electrocatalytic performance toward formic acid oxidation was tested in 0.5 M FA in 0.5 M $HClO_4$ aqueous solution from 0.05 to 1.1 V and ethanol oxidation in 0.5 M ethanol in 0.5 M NaOH aqueous solution in a potential window from −0.8 to 0.4 V (versus Hg/HgO), with a scanning rate of 50 mV $s^{-1}$, respectively. The chronoamperometric (CA) profiles were measured in 0.5 M FA in 0.5 M $HClO_4$ aqueous solution at a potential of 0.5 V (versus RHE) for 2000 s, and the CO stripping of nanocomposites was acquired in 0.5 M $HClO_4$ aqueous solution by following the procedures below; 0.5 M $HClO_4$ aqueous solution was first degassed with $N_2$ for 20 min. Then, CA measurements are acquired at 0.1 V (versus RHE) with the solution purged with CO for 5 min and then $N_2$ for another 20 min. Then, 2 CV scans were measured with a scan rate of 5 mV $s^{-1}$.

## RESULTS AND DISCUSSION

The sizes of Ru metal cores and Ru@Pt core−shell nanoparticles are first determined by TEM, and the size distribution histograms are shown in Figure S1. The size of both crystalline and amorphous Ru metal cores is about 2.5 nm, as shown in Figure S2a,b. Figure 1 displays the high-resolution TEM (HRTEM) images of Ru@Pt$_x$ core−shell nanoparticles that are evenly loaded on carbon nanotubes. The


DOI: 10.1021/acssuschemeng.9b01270
ACS Sustainable Chem. Eng. 2019, 7, 9007−9016

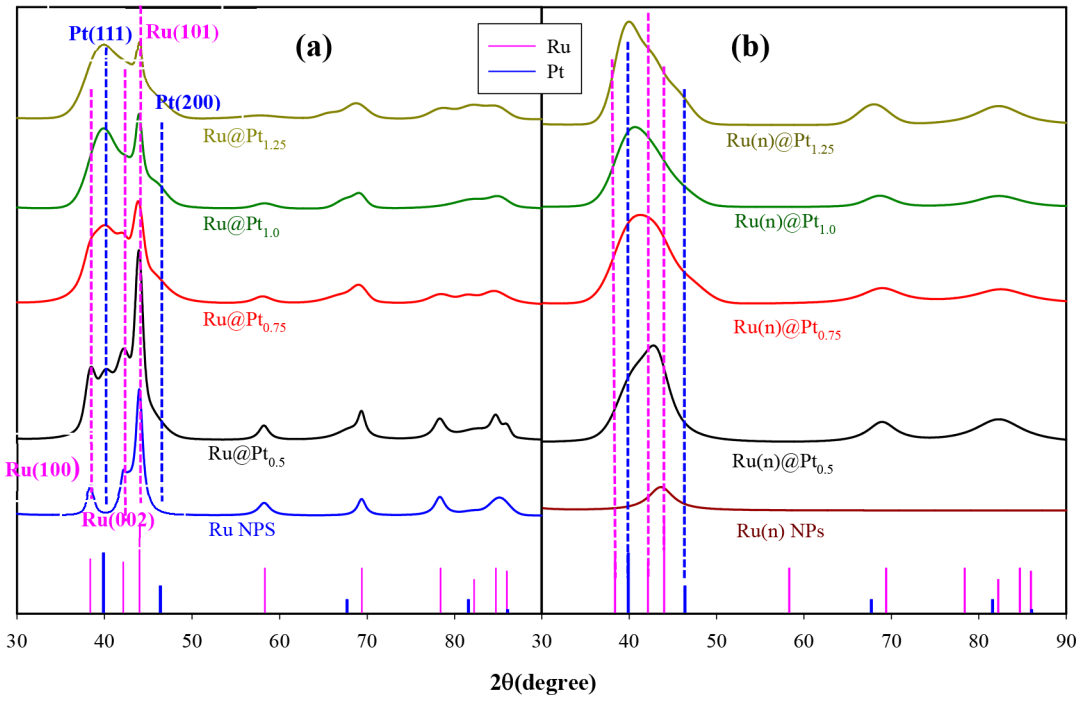


**Figure 3.** XRD profiles of (a) the annealed Ru NPs and Ru@Pt$_x$ core−shell nanoparticles and (b) as-prepared Ru(**n**) NPs and Ru(**n**)@Pt$_x$ core−shell nanoparticles. The detailed fitting process is exhibited in Figure S4.

size of Ru@Pt$_x$ core−shell nanoparticles is determined and shown in Table 1, which increased consistently with the atomic ratio of Pt to Ru. Since the size of crystalline and amorphous Ru metal cores is the same, it is anticipated that Ru@Pt$_x$ and Ru(**n**)@Pt$_x$ core−shell nanoparticles share the same size when the ratio of Pt to Ru is the same. As shown in Figure S2c, the diameter of Ru(**n**)@Pt$_{1.0}$ is 4.5 ± 0.5 nm, very close to that of Ru@Pt$_{1.0}$ (4.9 ± 0.7 nm, Figure 1c), in agreement with our anticipation. The same size of Ru(**n**)@Pt$_{1.0}$ and Ru@Pt$_{1.0}$ could rule out the size effect of Ru@Pt core−shell nanoparticles on the electronic and catalytic activity when evaluating the impact of the atomic ordering of the Ru core on the catalytic performance of Pt.[21] The core−shell structure of Ru@Pt$_x$ is well-confirmed by the HAADF-STEM images (Figure 1e), the line-scanning profile (Figure 1f), and energy-dispersive X-ray (EDX) elemental mapping (Figure 1g−i), which show that Ru elemental is located at the center while the Pt is at the exterior. The Pt shell thickness for Ru@Pt$_{1.0}$ is determined to be 1.3 nm from the line-scanning profile (Figure 1f). The Pt shell thickness can also be determined by TEM measurement, which is 0.7, 1.4, 2.4, and 4.3 nm, respectively, for $x$ = 0.5, 0.75, 1.0, and 1.25, corresponding to 1.2, 2.5, 4.3, and 7.7 layers of Pt. The Pt shell thickness determined from TEM measurements (1.2 nm) is in good agreement with that from the line-scanning profile (1.3 nm). It should be highlighted that the anisotropic growth of the Pt shell was observed on the crystalline Ru core, while Pt uniformly grows on amorphous Ru (Figure S2d).

For further confirmation of the formation of the Ru−Pt core−shell structure, instead of the Ru−Pt alloy on the Ru@Pt core−shell nanostructure, FTIR spectra of CO-adsorbed Ru@Pt$_x$ nanoparticles were measured and are shown in Figure 2. The CO vibrational bands adsorbed on Pt/C and Ru@Pt$_x$ nanoparticles are observed at around 2053 cm$^{-1}$,[18,28] while in contrast they showed up at 1930 cm$^{-1}$ on Ru/CNTs nanoparticles, suggesting the formation of the Ru@Pt core−shell structure. It should be noted that the vibrational band of CO adsorbed on Ru@Pt$_x$ core−shell nanoparticles shifted to a high frequency with the increasing thickness of Pt layers, probably because of less charge transfer from Pt to $\pi^*$ of CO induced by relieved compressive strain.[29]

The crystalline structure and Ru/Pt interface of Ru(**n**)@Pt$_x$ and Ru@Pt$_x$ nanoparticles are further characterized by XRD and further fitted with a Gaussian function by using Fityk software (Figure S4).[30] On the basis of the fitting results in Figure 3, the lattice parameters and lattice strain are calculated (Table 1). A well-defined crystalline hexagonal close-packed (hcp) phase is observed for annealed ruthenium cores in Figure 3a, with three inherent peaks of Ru (100), (002), and (101) facets appearing at 38.30°, 42.17°, and 42.94°, respectively. Ru@Pt$_{0.5}$ additionally shows a well-defined Pt (111) peak at 40.10° and a Pt (200) shoulder at 45.38° of face-centered cubic (fcc). When the Pt shell becomes thicker, the diffraction intensity of Pt (111) becomes more intense, and the diffraction peaks of Ru (100) and (002) are gradually overwhelmed by the peak of Pt (111). However, the diffraction peak of Ru (101) is still well-resolved even with the thick Pt shell and the diffraction peak position of Ru (101) staying consistent among all these samples. This suggests that Ru@Pt$_x$ core−shell NPs have well-defined boundaries, and no partial alloy of Pt−Ru was formed at the Ru−Pt interface.[31]

As shown in Figure 3b, amorphous Ru cores without thermal annealing show only a broad peak of Ru (101) at 43.64°, and no diffraction peaks of Ru (100) and (002) were observed, suggesting poor crystallinity and a highly disordered Ru metal core.[23] Ru(**n**)@Pt$_{0.5}$ core−shell nanoparticles showed a Ru(101) diffraction peak at 42.80°, which is shifted to lower diffraction angles relative to that of Ru(**n**) nanoparticles and which is indicative of lattice expansion due to Pt doping. Meanwhile, a shoulder at 40.40° that might be attributed to the Pt (111) and Pt (002) diffraction peak disappears. Such a weak diffraction peak for the Pt shell and



DOI: 10.1021/acssuschemeng.9b01270
ACS Sustainable Chem. Eng. 2019, 7, 9007−9016

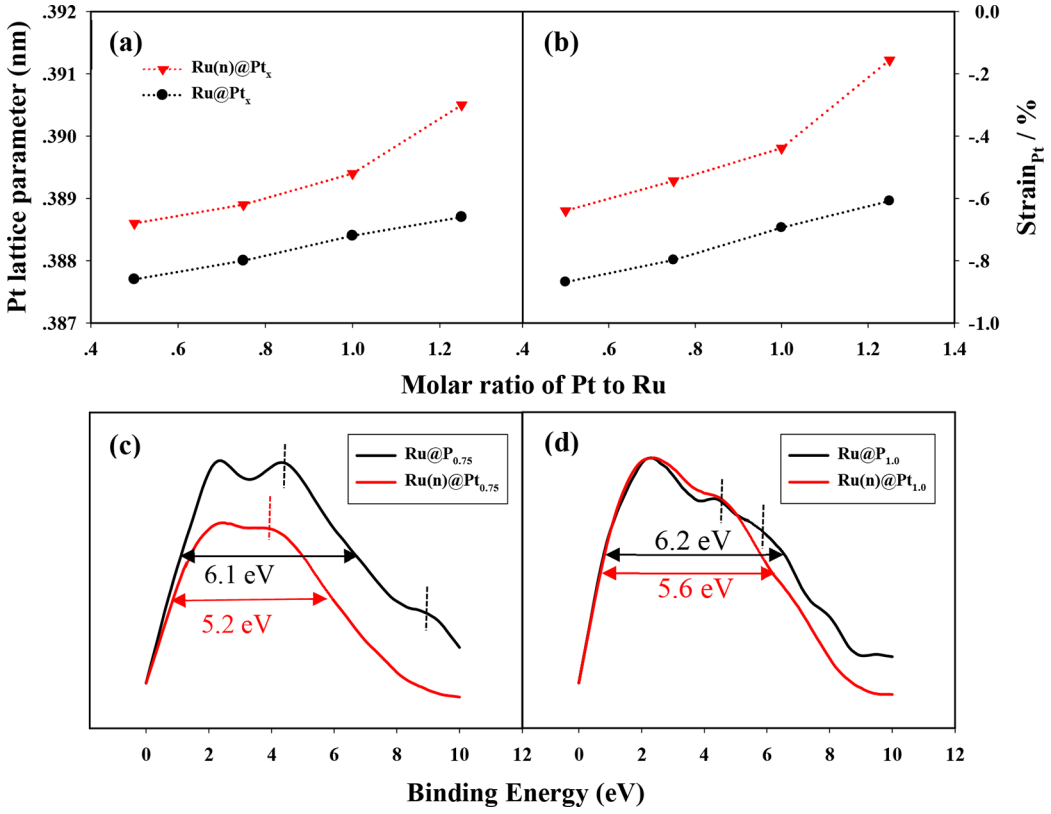


**Figure 4.** Dependence of (a) lattice constant and (b) lattice strain of the Pt shell on the molar ratio of Pt to Ru for Ru@Pt$_x$ and Ru(**n**)@Pt$_x$. Valence spectra of Ru@Pt$_x$ and Ru(**n**)@Pt$_x$, with $x$ = (c) 0.75 and (d) 1.0.

the shift of Ru(101) suggested the formation of a Ru-rich core and a Pt-rich Pt−Ru alloy shell for Ru(**n**)@Pt$_{0.5}$ nanoparticles, which might be promoted by the defect of the highly disordered Ru core.[31] The peak intensity of Pt(111) grows gradually with more coating of Pt, and a shoulder of Pt(200) become more prominent. Thus, it is highly possible that Pt atoms might grow on Pt−Ru alloy layers for Ru(**n**)@Pt$_x$ core−shell nanoparticles.

It has been widely accepted that the catalytic activity of metal nanoparticles is strongly dependent on the lattice strain of metal nanoparticles,[7] which could be induced through the core−shell structures. On the basis of the XRD measurements, the interplanar spacing ($d$) and lattice parameter $a$ of ($h$ $k$ $l$) facets of the Pt shell can be calculated via Bragg's law:

$$d = \frac{\lambda}{2\sin\theta} \quad (1)$$

$$a = d\sqrt{k^2 + l^2 + h^2} \quad (2)$$

Here, $\lambda$ is the incident X-ray wavelength ($\lambda$= 1.5418 Å), $\theta$ is the scattering angle, and ($h$ $k$ $l$) is the Miller index of the facets. Further, using

$$S_{Pt_{shell}} = \frac{a_{shell} - a_{Pt}}{a_{Pt}} \quad (3)$$

the strain of the Pt shell was obtained,[32] where $a_{shell}$ is the lattice parameter of the Pt shell, and $a_{Pt}$ is the lattice parameter of bulk Pt (JCPDS 87-0604). As shown in Table 1 and Figure 4a,b, the lattice parameters of the Pt shell increase while the strain of the Pt shell decreases for Ru@Pt$_x$ and Ru(**n**)@Pt$_x$ nanoparticles with the increase of the thickness of Pt. It should be noted that the lattice parameters and strain of the Pt shell of Ru(**n**)@Pt$_x$ change more drastically than those of Ru@Pt$_x$, suggesting that the Pt stacking on the highly disordered Ru core results in faster relaxation of the Pt strain with the increase of the Pt shell thickness.

It has been reported that the lattice strain might induce charge transfer between the metal core and shells, which further induces the shift of the binding energy and the d-band center of the catalyst.[33−35] Figure S5 shows the high-resolution XPS spectra for Pt 4f and Ru 3d for Ru@Pt$_x$ and Ru(**n**)@Pt$_x$. The binding energies of Pt 4f$_{7/2}$ and 4f$_{5/2}$ and are at 71.20 and 74.50 eV for Ru@Pt$_x$ and 71.30 and 74.7 eV for Ru(**n**)@Pt$_x$, which are attributed to the metallic Pt, as shown in Figure S5a,c. In Figure S5b,d, the Ru 3d$_{5/2}$ peaks for Ru@Pt$_x$ and Ru(**n**)@Pt$_x$ are observed at 280.3 and 280.4 eV, suggesting the metallic Ru. In addition, the peaks at around 285.85 and 288.9 eV originate from the C 1s of C−O and C−OO.[36] Therefore, there is no presence of oxidized Pt and Ru, and the binding energy of Pt 4f and Ru 3d stays constant when changing the Pt thickness. Interestingly, the ordering of the Ru metal core induces an apparent broadening of the d-band width and down-shift of the d-band center for Ru@Pt$_x$ core−shell nanoparticles. As shown in Figure 4c,d, the d-band width of Ru@Pt$_{0.75}$ (6.1 eV) is 0.9 eV larger than that of Ru(**n**)@Pt$_{0.75}$ (5.2 eV), and the d-band center of Ru@Pt$_{0.75}$ is about 0.4 eV lower than that of Ru(**n**)@Pt$_{0.75}$, although the d-band center of Ru@Pt$_{1.0}$ and Ru(**n**)@Pt$_{1.0}$ is almost the same. However, more sub-bands are observed for Ru@Pt$_{1.0}$ possibly because of the anisotropic growth of Pt on the crystalline Ru core,[37−39] which may result in more high-energy facets, vertices, and edges that are catalytically more active.[40−43]

The strain induced by the amorphous and crystalline Ru core is further evaluated by CO stripping voltammetry (Figure



DOI: 10.1021/acssuschemeng.9b01270
ACS Sustainable Chem. Eng. 2019, 7, 9007−9016

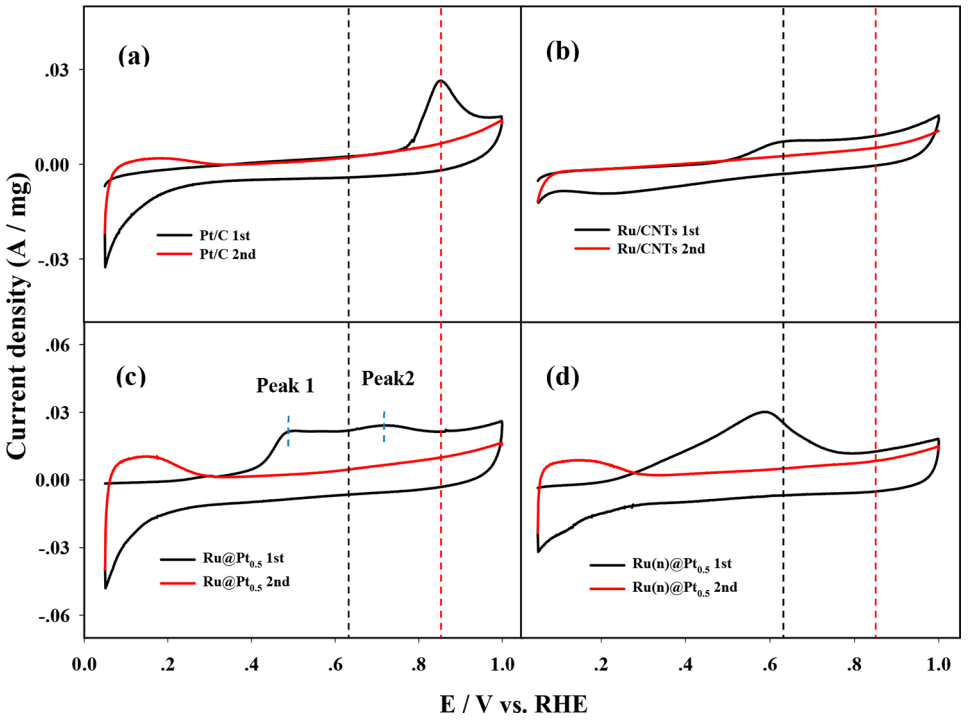


**Figure 5.** CO stripping voltammetry: (a) Pt/C, (b) Ru/CNTs, (c) Ru@$Pt_{0.5}$, (d) Ru(**n**)@$Pt_{0.5}$. The dashed black and red lines represent the potential for the CO stripping on Ru and Pt, respectively.

5 and Figure S6). The CO stripping potentials for Pt/C and Ru/CNTs are observed at 0.85 and 0.63 V, respectively, in agreement with previously well-established results.[14,44] Interestingly, all Ru@$Pt_x$ and Ru(**n**)@$Pt_x$ samples except Ru(**n**)@$Pt_{0.5}$ display two CO oxidation peaks, which are assigned to the two states of Pt atoms on the Pt shell induced by the Ru core,[24,45,46] while only one CO stripping peak was observed for Ru(**n**)@$Pt_{0.5}$ suggesting the formation of the Pt−Ru alloy when a thin layer of Pt is deposited on the amorphous Ru core.[44] As displayed in Table 2, the two CO stripping peak potentials for Ru@$Pt_x$ and Ru(**n**)@$Pt_x$ samples are much lower than that of Pt/C and increase with the Pt shell thickness, suggesting that the d-band center of the Pt shell is reduced by the compressive strain induced by the Ru core, which attenuates with the increase of the Pt shell thickness. In addition, the CO stripping potential of Ru@$Pt_x$ and Ru(**n**)@$Pt_x$ induced by the crystalline Ru core is apparently smaller than that by amorphous one, further suggesting that the more compressive strain and down-shift of the d-band center is induced by the former as compared to the latter. These results are in good agreement with those derived from XRD and photoelectron spectroscopy analysis.

**Table 2. CO Stripping Peak Potential for Ru@$Pt_x$ and Ru(n)@$Pt_x$**

| | | potential/V | | | |
|---|---|---|---|---|---|
| catalyst | peak | $x$ = 0.5 | $x$ = 0.75 | $x$ = 1.0 | $x$ = 1.25 |
| Ru@$Pt_x$ | peak 1 | 0.48 | 0.51 | 0.54 | 0.59 |
| | peak 2 | 0.72 | 0.74 | 0.78 | 0.82 |
| Ru(n)@$Pt_x$ | peak 1 | 0.58 | 0.58 | 0.59 | 0.59 |
| | peak 2 | | 0.79 | 0.81 | 0.84 |

| catalyst | potential/V |
|---|---|
| Pt/C | 0.85 |
| Ru/CNTs | 0.63 |

**Electrochemical Performance toward Formic Acid Oxidation.** The impact of the disordering of the Ru metal core on the catalytic activity of Ru@$Pt_x$ and Ru(**n**)@$Pt_x$ toward formic acid and ethanol oxidation was further investigated and discussed in terms of lattice strain. The ECSA values of Pt/C, Ru@$Pt_x$, and Ru(**n**)@$Pt_x$ are derived from the CV (Figure S7) in 0.5 M $HClO_4$ aqueous solution by using the underpotential hydrogen desorption ($H_{upd}$)[27] from 0.05 to 0.4 V, and the catalytic activity is characterized by CV in 0.5 M FA + 0.5 M $HClO_4$ (Figure 6 and Figure S8). A dual-pathway mechanism has been proposed for FA oxidation on Pt: the dehydrogenation and dehydration pathway.[42,47,48] The dehydrogenation pathway involves direct oxidation of FA to $CO_2$, while the dehydration pathway produces CO poisoning species which can only be oxidized at high potential (>0.7 V).[49] As shown in Table S2, two oxidation peaks are observed at 0.5 and 0.93 V for Pt/C, which are ascribed to the direct oxidation of FA and the oxidation of poisonous intermediates from indirect FA oxidation.[50,51] Compared to that of Pt/C, no apparent peak potential shift was observed for Ru@$Pt_x$ and Ru(**n**)@$Pt_x$ samples, but their catalytic activity is markedly enhanced. In addition, the enhanced catalytic activity by the crystalline Ru core is much higher than that of the amorphous Ru core, and a volcano-shape dependence of the specific activity of Ru(**n**)@$Pt_x$ and Ru@$Pt_x$ nanoparticles on the molar ratio of Pt to Ru and lattice strain of Pt was observed (Figure 7), suggesting a remarkable impact of the crystalline Ru core and thickness of the Pt shell on the catalytic activity of core−shell nanostructures. The compressive strain results in a down-shift of the d-band center of the Pt shell, thus reducing the adsorption energy of poisonous species (Figure 6) and alleviating the catalyst poisoning by the CO species (Table 2). Since the CO stripping potential on Ru@$Pt_x$ is much lower


DOI: 10.1021/acssuschemeng.9b01270
ACS Sustainable Chem. Eng. 2019, 7, 9007−9016

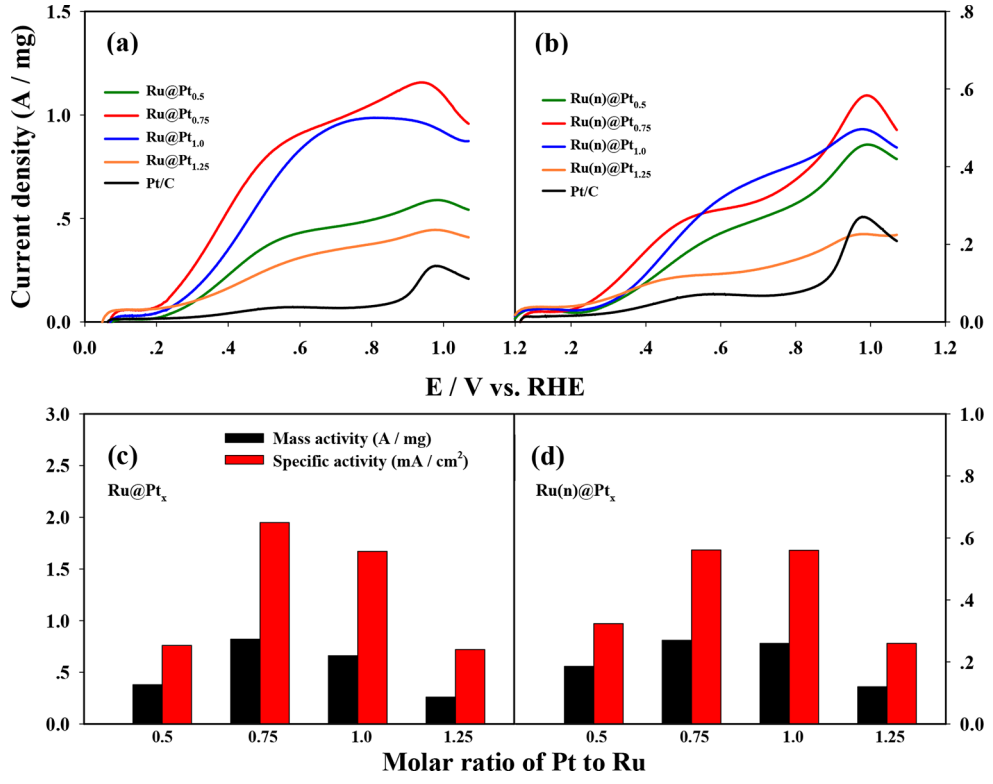


**Figure 6.** Forward CV scans of (a) Ru@$Pt_x$ and (b) Ru(**n**)@$Pt_x$ ($x$ = 0.5, 0.75, 1.0, and 1.25) in 0.5 M $HClO_4$ and 0.5 M HCOOH with a sweep rate of 50 mV $s^{-1}$. Dependence of the mass activity and specific activity of direct oxidation ($i_{p1}$) of (c) Ru@$Pt_x$ and (d) Ru(**n**)@$Pt_x$ nanoparticles on the molar ratio of Pt to Ru.

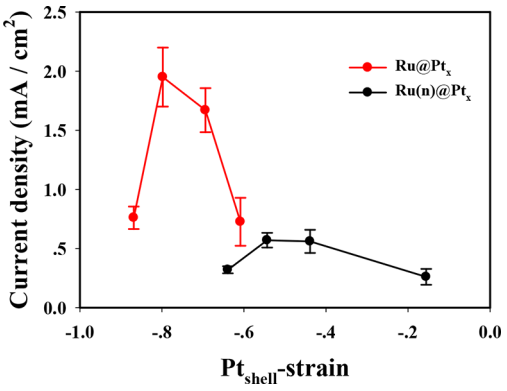


**Figure 7.** Dependence of the specific activity of Ru(**n**)@$Pt_x$ and Ru@$Pt_x$ nanoparticles on the lattice strain of the Pt shell.

than that on Ru(**n**)@$Pt_x$ samples, less poisoning and higher catalytic activity for Ru@$Pt_x$ are observed as compared to Ru(**n**)@$Pt_x$. As demonstrated in Table S2, the ratio of $i_{p1}$ to $i_{p2}$ for Ru@$Pt_x$ is apparently larger than that for Ru(**n**)@$Pt_x$, indicating less of the poisoning effect for Ru@$Pt_x$ than for Ru(**n**)@$Pt_x$, in agreement with the conclusion derived from the CO stripping. However, the down-shift of the d-band center also reduces the adsorption energy and surface coverage of formic acid on the catalyst and further lowers the catalytic activity. Only when the two effects are well-balanced can Ru@$Pt_x$ and Ru(**n**)@$Pt_x$ samples achieve the best catalytic performances, and thus, a volcano-shape dependence of the catalytic activity on the strain was observed.

The stabilities of Pt/C, Ru@$Pt_x$, and Ru(**n**)@$Pt_x$ samples are evaluated by CA measurements at 0.5 V in Figure S8c,d. It is noticed that Ru(**n**)@$Pt_x$ shows a very fast decay of current density in the initial 500 s and then a slow deactivation process in the remaining 1500 s. Instead, Ru@$Pt_x$ samples show a much slowed deactivation process and are more CO-tolerant than Ru(**n**)@$Pt_x$, in agreement with the results derived from CO stripping. Among all these samples, Ru@$Pt_{1.0}$ exhibits the highest mass activity of 0.12 A $mg^{-1}$ after 2000 s of CA measurement, which is almost 3.3 times that of Ru(**n**)@$Pt_{1.0}$ (0.036 A $mg^{-1}$) and 15 times that of Pt/C. The CV scans of both Ru@$Pt_x$ and Ru(**n**)@$Pt_x$ nanoparticles in 0.5 M $HClO_4$ after 2000 s of CA measurements at 0.5 V in 0.5 M FA + 0.5 M $HClO_4$ are shown in Figure S9. However, no CO stripping feature is observed, suggesting that the deactivation process of Ru@$Pt_x$ and Ru(**n**)@$Pt_x$ are caused by other organic intermediates, instead of CO. Additionally, the structure stability of Ru@$Pt_x$ and Ru(**n**)@$Pt_x$ catalysts also was evaluated by measuring the ECSA of the catalyst before and after CA measurements for 4 h at 0.5 V (versus RHE). As shown in Figure S10, Ru(**n**)@$Pt_x$ shows a loss of ECSA, which decreases with the Pt shell thickness. However, Ru@$Pt_x$ demonstrated a minimum change of ECSA during such a measurement, suggesting a more stable nanostructure than Ru(**n**)@$Pt_x$.

**Electrochemical Oxidation toward Ethanol.** The catalytic activity of Ru@$Pt_x$, Ru(**n**)@$Pt_x$ and Pt/C toward ethanol are further studied.

According to the previous reports, the oxidation of ethanol involves two reaction mechanisms ($C_1$-pathway and $C_2$-pathway) in alkaline solution. In the $C_1$-pathway, ethanol is oxidized into carbonate ($CO_3^{-}$) directly or via a $CO_{ads}$ intermediate by transferring 12 electrons, while in the $C_2$-pathway, ethanol is oxidized through a 4-electron transfer and


DOI: 10.1021/acssuschemeng.9b01270
ACS Sustainable Chem. Eng. 2019, 7, 9007−9016

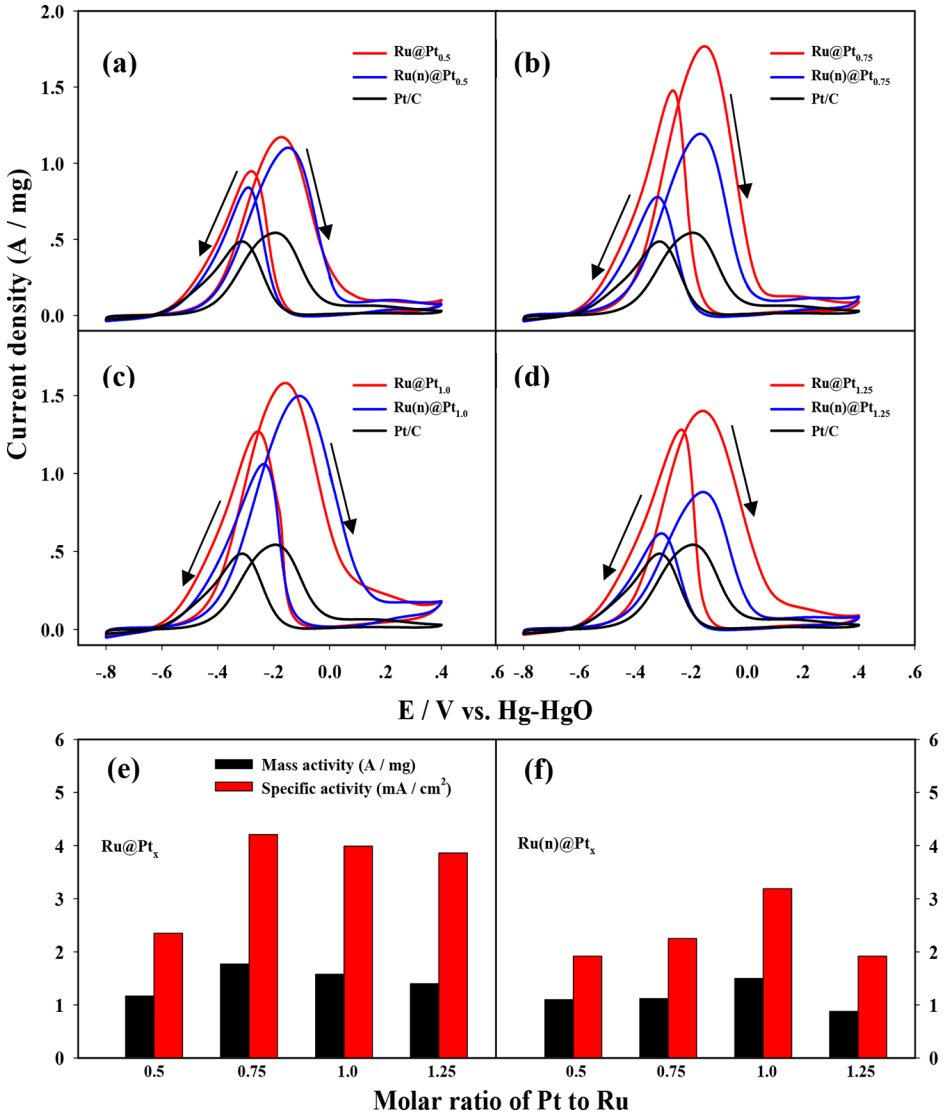


**Figure 8.** CV scans of Pt/C, Ru@Pt$_x$, and Ru(**n**)@Pt$_x$: $x$ = (a) 0.5, (b) 0.75, (c) 1.0, and (d) 1.25 in 0.5 M ethanol in 0.5 M NaOH aqueous solution with a scanning rate of 50 mV s$^{-1}$. Bar charts of mass activity and specific activity of (e) Ru@Pt$_x$ and (f) Ru(**n**)Pt$_x$.

produces acetaldehyde and acetate.[52,53] Figure 8a–d shows the CV scans of Ru@Pt$_x$, Ru(**n**)@Pt$_x$, and Pt/C in 0.5 M ethanol in 0.5 M NaOH aqueous solution, and the redox peaks in positive and negative scans are attributed to the formation of $CO_3^-$ and $CH_3CHOO^-$, respectively.[53,54] Both the mass activity and specific activity of Ru@Pt$_x$ and Ru(**n**)@Pt$_x$ samples derived from Figure 8a–d are shown in Figure 8e,f, and a volcano-shape dependence on the ratio of Pt to Ru is observed. Among all these catalysts, Ru@Pt$_{0.75}$ demonstrates the highest performance, with a specific activity of 4.21 mA cm$^{-2}$, 6.5 times that of Pt/C and 1.8 times that of Ru(**n**)@Pt$_{0.75}$. Different from the behavior toward formic acid oxidation, Ru@Pt$_x$ samples deliver only slightly higher activity than Ru(**n**)@Pt$_x$, since the weaker binding energy of CO as compared to hydroxyl radicals induced by the compressive strain of Pt catalyst in alkaline solution promotes CO oxidation and alleviates CO poisoning.[55] The potential cycling durabilities of Ru@Pt$_x$ and Ru(**n**)@Pt$_x$ are shown in Figure S11, where the highest mass activities of Ru@Pt$_x$ and Ru(**n**)@Pt$_x$ samples after 240 cycles are achieved by Ru@Pt$_{1.0}$ and Ru(**n**)@Pt$_{1.0}$, delivering a mass activity of 0.77 and 0.65 A mg$^{-1}$ and an attenuation rate of 19.7% and 40.9%, respectively.

## CONCLUSION

In summary, we have successfully synthesized Ru@Pt core–shell NPs with both amorphous and highly crystalline Ru cores, which were characterized by XRD, STEM, XPS, and CO stripping. The ordered Ru core resulted in a well-defined heterostructure at the Ru–Pt interface, more apparent lattice strain on the Pt shell, and a down-shift of the d-band center as compared to the amorphous Ru core, which further induces more reduction of the CO adsorption energy, Pt poisoning, and more enhanced catalytic activity of Ru@Pt toward formic acid and ethanol oxidation by the crystalline Ru core. Among all these catalysts, Ru@Pt$_{0.75}$ exhibits the highest specific activity of 1.95 mA cm$^{-2}$ toward the direct oxidation of formic acid and 4.21 mA cm$^{-2}$ for direct ethanol oxidation, which are 25 and 6.5 times those of Pt/C, and 3.4 and 1.8 times those of Ru(**n**)@Pt$_{0.75}$, respectively. Ru@Pt$_{0.75}$ also delivers a mass activity of 0.82 and 1.77 A mg$^{-1}$ toward formic acid oxidation and ethanol oxidation, 12 and 3.3 times those of Pt/C, and 3.0


DOI: 10.1021/acssuschemeng.9b01270
ACS Sustainable Chem. Eng. 2019, 7, 9007–9016

and 1.6 times those of Ru(n)@$Pt_{0.75}$, respectively. Such a superior performance of Ru@$Pt_x$ as compared to Ru(n)@$Pt_x$ is ascribed to the reduced d-band center and weaker CO adsorption induced by the highly crystalline Ru core and appropriate lattice strain of the Pt shell. This work may shed light on the rational design of superior and cost-efficient electrocatalysts in the future for the direct small organic molecule fuel cell.

## ■ ASSOCIATED CONTENT

### Supporting Information

The Supporting Information is available free of charge on the ACS Publications website at DOI: 10.1021/acssuschemeng.9b01270.

Detailed experimental sections, size distribution histograms, FTIR, detailed XRD deconvolution profiles, XPS full surveys, and CO striping measurements (PDF)

## ■ AUTHOR INFORMATION


### Corresponding Author

*E-mail: esxkang@scut.edu.cn.

### ORCID

Xiongwu Kang: 0000-0003-2587-4962

Shaowei Chen: 0000-0002-3668-8551


### Notes

The authors declare no competing financial interest.

§E-mail: shaowei@ucsc.edu.

## ■ ACKNOWLEDGMENTS

This work was supported by the National Natural Science Foundation of China (51602106) and Guangdong Innovative and Entrepreneurial Research Team Program (2016ZT06N569).

## ■ REFERENCES


(1) Chen, A.; Holt-Hindle, P. Platinum-Based Nanostructured Materials: Synthesis, Properties, and Applications. *Chem. Rev.* **2010**, *110* (6), 3767−3804.

(2) Cao, M.; Wu, D.; Cao, R. Recent Advances in the Stabilization of Platinum Electrocatalysts for Fuel-Cell Reactions. *ChemCatChem* **2014**, *6* (1), 26−45.

(3) Leong, G. J.; Schulze, M. C.; Strand, M. B.; Maloney, D.; Frisco, S. L.; Dinh, H. N.; Pivovar, B.; Richards, R. M. Shape-Directed Platinum Nanoparticle Synthesis: Nanoscale Design of Novel Catalysts. *Appl. Organomet. Chem.* **2014**, *28* (1), 1−17.

(4) Wee, J. H.; Lee, K. Y. Overview of the Development of CO-Tolerant Anode Electrocatalysts for Proton-Exchange Membrane Fuel Cells. *J. Power Sources* **2006**, *157* (1), 128−135.

(5) Kakati, N.; Maiti, J.; Lee, S. H.; Jee, S. H.; Viswanathan, B.; Yoon, Y. S. Anode Catalysts for Direct Methanol Fuel Cells in Acidic Media: Do We Have Any Alternative for Pt or Pt-Ru? *Chem. Rev.* **2014**, *114* (24), 12397−12429.

(6) Scott, F. J.; Roth, C.; Ramaker, D. E. Kinetics of CO Poisoning in Simulated Reformate and Effect of Ru Island Morphology on PtRu Fuel Cell Catalysts as Determined by Operando X-ray Absorption Near Edge Spectroscopy. *J. Phys. Chem. C* **2007**, *111* (30), 11403−11413.

(7) Luo, M. C.; Guo, S. J. Strain-Controlled Electrocatalysis on Multimetallic Nanomaterials. *Nat. Rev. Mater.* **2017**, *2* (11), 17059.

(8) Roth, C.; Benker, N.; Theissmann, R.; Nichols, R. J.; Schiffrin, D. J. Bifunctional Electrocatalysis in Pt-Ru Nanoparticle Systems. *Langmuir* **2008**, *24* (5), 2191−9.

(9) Roth, C.; Papworth, A. J.; Hussain, I.; Nichols, R. J.; Schiffrin, D. J. A Pt/Ru Nanoparticulate System to Study the Bifunctional Mechanism of Electrocatalysis. *J. Electroanal. Chem.* **2005**, *581* (1), 79−85.

(10) Antolini, E. The Problem of Ru Dissolution from Pt−Ru Catalysts During Fuel Cell Operation: Analysis and Solutions. *J. Solid State Electrochem.* **2011**, *15* (3), 455−472.

(11) Henry, P. A.; Guétaz, L.; Pélissier, N.; Jacques, P. A.; Escribano, S. Structural and Chemical Analysis by Transmission Electron Microscopy of Pt−Ru Membrane Precipitates in Proton Exchange Membrane Fuel Cell Aged under Reformate. *J. Power Sources* **2015**, *275*, 312−321.

(12) Park, G. S.; Pak, C.; Chung, Y. S.; Kim, J. R.; Jeon, W. S.; Lee, Y. H.; Kim, K.; Chang, H.; Seung, D. Decomposition of Pt−Ru Anode Catalysts in Direct Methanol Fuel Cells. *J. Power Sources* **2008**, *176* (2), 484−489.

(13) Guo, J. S.; Sun, G. Q.; Wu, Z. M.; Sun, S. G.; Yan, S. Y.; Cao, L.; Yan, Y. S.; Su, D. S.; Xin, Q. The Durability of Polyol-Synthesized PtRu/C for Direct Methanol Fuel Cells. *J. Power Sources* **2007**, *172* (2), 666−675.

(14) Ochal, P.; de la Fuente, J. L. G.; Tsypkin, M.; Seland, F.; Sunde, S.; Muthuswamy, N.; Ronning, M.; Chen, D.; Garcia, S.; Alayoglu, S.; Eichhorn, B. CO Stripping as an Electrochemical Tool for Characterization of Ru@Pt Core-Shell Catalysts. *J. Electroanal. Chem.* **2011**, *655* (2), 140−146.

(15) Schlapka, A.; Lischka, M.; Gross, A.; Kasberger, U.; Jakob, P. Surface Strain versus Substrate Interaction in Heteroepitaxial Metal Layers: Pt on Ru(0001). *Phys. Rev. Lett.* **2003**, *91* (1), 016101.

(16) Hartmann, H.; Diemant, T.; Bansmann, J.; Behm, R. J. Interaction of CO and Deuterium with Bimetallic, Monolayer Pt-Island/Film Covered Ru(0001) Surfaces. *Phys. Chem. Chem. Phys.* **2012**, *14* (31), 10919−34.

(17) Wang, J. J.; Liu, Y. T.; Chen, I.; Yang, Y. W.; Yeh, T. K.; Lee, C. H.; Hu, C. C.; Wen, T. C.; Chen, T. Y.; Lin, T. L. Near-Monolayer Platinum Shell on Core−Shell Nanocatalysts for High-Performance Direct Methanol Fuel Cell. *J. Phys. Chem. C* **2014**, *118* (5), 2253−2262.

(18) Alayoglu, S.; Nilekar, A. U.; Mavrikakis, M.; Eichhorn, B. Ru-Pt Core-Shell Nanoparticles for Preferential Oxidation of Carbon Monoxide in Hydrogen. *Nat. Mater.* **2008**, *7* (4), 333−8.

(19) Kaplan, D.; Alon, M.; Burstein, L.; Rosenberg, Y.; Peled, E. Study of Core−Shell Platinum-Based Catalyst for Methanol and Ethylene Glycol Oxidation. *J. Power Sources* **2011**, *196* (3), 1078−1083.

(20) Zhang, L.; Kim, J.; Chen, H. M.; Nan, F.; Dudeck, K.; Liu, R. S.; Botton, G. A.; Zhang, J. A Novel CO-Tolerant PtRu Core−Shell Structured Electrocatalyst with Ru Rich in Core and Pt Rich in Shell for Hydrogen Oxidation Reaction and its Implication in Proton Exchange Membrane Fuel Cell. *J. Power Sources* **2011**, *196* (22), 9117−9123.

(21) Goto, S.; Hosoi, S.; Arai, R.; Tanaka, S.; Umeda, M.; Yoshimoto, M.; Kudo, Y. Particle-Size- and Ru-Core-Induced Surface Electronic States of Ru-Core/Pt-Shell Electrocatalyst Nanoparticles. *J. Phys. Chem. C* **2014**, *118* (5), 2634−2640.

(22) Gawande, M. B.; Goswami, A.; Asefa, T.; Guo, H.; Biradar, A. V.; Peng, D. L.; Zboril, R.; Varma, R. S. Core-Shell Nanoparticles: Synthesis and Applications in Catalysis and Electrocatalysis. *Chem. Soc. Rev.* **2015**, *44* (21), 7540−90.

(23) Alayoglu, S.; Zavalij, P.; Eichhorn, B.; Wang, Q.; Frenkel, A. I.; Chupas, P. Structural and Architectural Evaluation of Bimetallic Nanoparticles: A Case Study of Pt-Ru Core-Shell and Alloy Nanoparticles. *ACS Nano* **2009**, *3* (10), 3127−37.

(24) El Sawy, E. N.; Pickup, P. G. Formic Acid Oxidation at Ru@Pt Core-Shell Nanoparticles. *Electrocatalysis* **2016**, *7* (6), 477−485.

(25) Nilekar, A. U.; Alayoglu, S.; Eichhorn, B.; Mavrikakis, M. Preferential CO oxidation in Hydrogen: Reactivity of Core-Shell Nanoparticles. *J. Am. Chem. Soc.* **2010**, *132* (21), 7418−28.

(26) Lu, S. L.; Eid, K.; Ge, D. H.; Guo, J.; Wang, L.; Wang, H. J.; Gu, H. W. One-pot Synthesis of PtRu Nanodendrites as Efficient Catalysts for Methanol Oxidation Reaction. *Nanoscale* **2017**, *9* (3), 1033−1039.




DOI: 10.1021/acssuschemeng.9b01270
*ACS Sustainable Chem. Eng.* 2019, 7, 9007−9016

(27) Shao, Y. Y.; Yin, G. P.; Wang, H. H.; Gao, Y. Z.; Shi, P. F. Multi-Walled Carbon Nanotubes Based Pt Electrodes Prepared with in Situ Ion Exchange Method for Oxygen Reduction. *J. Power Sources* **2006**, *161* (1), 47−53.
(28) Maillard, F.; Bonnefont, A.; Chatenet, M.; Guetaz, L.; Doisneati-Cottignies, B.; Roussel, H.; Stimming, U. Effect of the Structure of Pt-Ru/C Particles on $CO_{ad}$ Monolayer Vibrational Properties and Electrooxidation Kinetics. *Electrochim. Acta* **2007**, *53* (2), 811−822.
(29) Jakob, P.; Schlapka, A. CO Adsorption on Epitaxially Grown Pt Layers on Ru (0001). *Surf. Sci.* **2007**, *601* (17), 3556−3568.
(30) Luo, Y.; Calvillo, L.; Daiguebonne, C.; Daletou, M. K.; Granozzi, G.; Alonso-Vante, N. A Highly Efficient and Stable Oxygen Reduction Reaction on Pt/$CeO_x$/C Electrocatalyst Obtained via a Sacrificial Precursor Based on a Metal-Organic Framework. *Appl. Catal., B* **2016**, *189*, 39−50.
(31) Hsieh, Y.-C.; Zhang, Y.; Su, D.; Volkov, V.; Si, R.; Wu, L.; Zhu, Y.; An, W.; Liu, P.; He, P.; Ye, S.; Adzic, R. R.; Wang, J. X. Ordered Bilayer Ruthenium−Platinum Core-Shell Nanoparticles as Carbon Monoxide-Tolerant Fuel Cell Catalysts. *Nat. Commun.* **2013**, *4*, 2466.
(32) Strasser, P.; Koh, S.; Anniyev, T.; Greeley, J.; More, K.; Yu, C.; Liu, Z.; Kaya, S.; Nordlund, D.; Ogasawara, H.; Toney, M. F.; Nilsson, A. Lattice-Strain Control of the Activity in Dealloyed Core-Shell Fuel Cell Catalysts. *Nat. Chem.* **2010**, *2* (6), 454−60.
(33) Wang, W.; Lv, F.; Lei, B.; Wan, S.; Luo, M.; Guo, S. Tuning Nanowires and Nanotubes for Efficient Fuel-Cell Electrocatalysis. *Adv. Mater.* **2016**, *28* (46), 10117−10141.
(34) Luo, M.; Sun, Y.; Zhang, X.; Qin, Y.; Li, M.; Li, Y.; Li, C.; Yang, Y.; Wang, L.; Gao, P.; Lu, G.; Guo, S. Stable High-Index Faceted Pt Skin on Zigzag-Like PtFe Nanowires Enhances Oxygen Reduction Catalysis. *Adv. Mater.* **2018**, *30* (10), 1705515.
(35) Bu, L.; Guo, S.; Zhang, X.; Shen, X.; Su, D.; Lu, G.; Zhu, X.; Yao, J.; Guo, J.; Huang, X. Surface Engineering of Hierarchical Platinum-Cobalt Nanowires for Efficient Electrocatalysis. *Nat. Commun.* **2016**, *7*, 11850.
(36) Okpalugo, T. I. T.; Papakonstantinou, P.; Murphy, H.; McLaughlin, J.; Brown, N. M. D. High Resolution XPS Characterization of Chemical Functionalised MWCNTs and SWCNTs. *Carbon* **2005**, *43* (1), 153−161.
(37) Kang, Y. Q.; Xue, Q.; Peng, R. L.; Jin, P. J.; Zeng, J. H.; Jiang, J. X.; Chen, Y. Bimetallic AuRh Nanodendrites Consisting of Au Icosahedron Cores and Atomically Ultrathin Rh Nanoplate Shells: Synthesis and Light-Enhanced Catalytic Activity. *NPG Asia Mater.* **2017**, *9*, e407.
(38) Li, F. M.; Ding, Y.; Xiao, X.; Yin, S. B.; Hu, M. C.; Li, S. N.; Chen, Y. From Monometallic Au Nanowires to Trimetallic AuPtRh Nanowires: Interface Control for the Formic Acid Electrooxidation. *J. Mater. Chem. A* **2018**, *6* (35), 17164−17170.
(39) Kang, Y. Q.; Xue, Q.; Zhao, Y.; Li, X. F.; Jin, P. J.; Chen, Y. Selective Etching Induced Synthesis of Hollow Rh Nanospheres Electrocatalyst for Alcohol Oxidation Reactions. *Small* **2018**, *14* (29), e1801239.
(40) Sheng, T.; Tian, N.; Zhou, Z. Y.; Lin, W. F.; Sun, S. G. Designing Pt-Based Electrocatalysts with High Surface Energy. *ACS Energy Lett.* **2017**, *2* (8), 1892−1900.
(41) Zhang, B. W.; Zhang, Z. C.; Liao, H. G.; Gong, Y.; Gu, L.; Qu, X. M.; You, L. X.; Liu, S.; Huang, L.; Tian, X. C.; Huang, R.; Zhu, F. C.; Liu, T.; Jiang, Y. X.; Zhou, Z. Y.; Sun, S. G. Tuning Pt-Skin to Ni-Rich Surface of Pt3Ni Catalysts Supported on Porous Carbon for Enhanced Oxygen Reduction Reaction and Formic Electro-Oxidation. *Nano Energy* **2016**, *19*, 198−209.
(42) Sheng, T.; Xu, Y. F.; Jiang, Y. X.; Huang, L.; Tian, N.; Zhou, Z. Y.; Broadwell, I.; Sun, S. G. Structure Design and Performance Tuning of Nanomaterials for Electrochemical Energy Conversion and Storage. *Acc. Chem. Res.* **2016**, *49* (11), 2569−2577.
(43) Huang, L.; Sun, J. Y.; Cao, S. H.; Zhan, M.; Ni, Z. R.; Sun, H. J.; Chen, Z.; Zhou, Z. Y.; Sorte, E. G.; Tong, Y. Y. J.; Sun, S. G. Combined EC-NMR and In Situ FTIR Spectroscopic Studies of Glycerol Electrooxidation on Pt/C, PtRu/C, and PtRh/C. *ACS Catal.* **2016**, *6* (11), 7686−7695.
(44) Muthuswamy, N.; de la Fuente, J. L. G.; Tran, D. T.; Walmsley, J.; Tsypkin, M.; Raaen, S.; Sunde, S.; Rønning, M.; Chen, D. Ru@Pt Core−Shell Nanoparticles for Methanol Fuel Cell Catalyst: Control and Effects of Shell Composition. *Int. J. Hydrogen Energy* **2013**, *38* (36), 16631−16641.
(45) El Sawy, E. N.; El-Sayed, H. A.; Birss, V. I. Novel Electrochemical Fingerprinting Methods for the Precise Determination of Pt(shell) Coverage on Ru(core) Nanoparticles. *Chem. Commun.* **2014**, *50* (78), 11558−61.
(46) Schwammlein, J. N.; Stuhmeier, B. M.; Wagenbauer, K.; Dietz, H.; Tileli, V.; Gasteiger, H. A.; El-Sayed, H. A. Origin of Superior HOR/HER Activity of Bimetallic Pt-Ru Catalysts in Alkaline Media Identified via Ru@Pt Core-Shell Nanoparticles. *J. Electrochem. Soc.* **2018**, *165* (5), H229−H239.
(47) Duan, T.; Zhang, R. G.; Ling, L. X.; Wang, B. J. Insights into the Effect of Pt Atomic Ensemble on HCOOH Oxidation over Pt-Decorated Au Bimetallic Catalyst To Maximize Pt Utilization. *J. Phys. Chem. C* **2016**, *120* (4), 2234−2246.
(48) Chen, Q. S.; Zhou, Z. Y.; Vidal-Iglesias, F. J.; Solla-Gullon, J.; Feliu, J. M.; Sun, S. G. Significantly Enhancing Catalytic Activity of Tetrahexahedral Pt Nanocrystals by Bi Adatom Decoration. *J. Am. Chem. Soc.* **2011**, *133* (33), 12930−3.
(49) Zhou, Y. Y.; Liu, C. H.; Liu, J.; Cai, X. L.; Lu, Y.; Zhang, H.; Sun, X. H.; Wang, S. D. Self-Decoration of PtNi Alloy Nanoparticles on Multiwalled Carbon Nanotubes for Highly Efficient Methanol Electro-Oxidation. *Nano-Micro Lett.* **2016**, *8* (4), 371−380.
(50) Liao, M. Y.; Li, W. P.; Xi, X. P.; Luo, C. L.; Gui, S. L.; Jiang, C.; Mai, Z. H.; Chen, B. H. Highly Active Au-Core@Pt-Cluster Catalyst for Formic Acid Electrooxidation. *J. Electroanal. Chem.* **2017**, *791*, 124−130.
(51) Obradović, M. D.; Rogan, J. R.; Babić, B. M.; Tripković, A. V.; Gautam, A. R. S.; Radmilović, V. R.; Gojković, S. L. Formic Acid Oxidation on Pt−Au Nanoparticles: Relation Between the Catalyst Activity and the Poisoning Rate. *J. Power Sources* **2012**, *197*, 72−79.
(52) Wang, Y.; Zou, S. Z.; Cai, W. B. Recent Advances on Electro-Oxidation of Ethanol on Pt- and Pd-Based Catalysts: From Reaction Mechanisms to Catalytic Materials. *Catalysts* **2015**, *5* (3), 1507−1534.
(53) Ma, L.; Chu, D.; Chen, R. R. Comparison of Ethanol Electro-Oxidation on Pt/C and Pd/C Catalysts in Alkaline Media. *Int. J. Hydrogen Energy* **2012**, *37* (15), 11185−11194.
(54) Jiang, L.; Hsu, A.; Chu, D.; Chen, R. Ethanol Electro-Oxidation on Pt/C and PtSn/C Catalysts in Alkaline and Acid Solutions. *Int. J. Hydrogen Energy* **2010**, *35* (1), 365−372.
(55) Choi, I.; Lim, D.-H.; Shin, D. Y. Highly Dispersed and $CO_{ad}$-Tolerant Pt Shell -Pd Core Catalyst for Ethanol Oxidation Reaction: Catalytic Activity and Long-Term Durability. *Int. J. Hydrogen Energy* **2018**, *43* (24), 11335−11344.


DOI: 10.1021/acssuschemeng.9b01270
*ACS Sustainable Chem. Eng.* 2019, 7, 9007−9016